Super-resolution characterization of heterogeneous light-matter interactions between single dye molecules and plasmonic nanoparticles

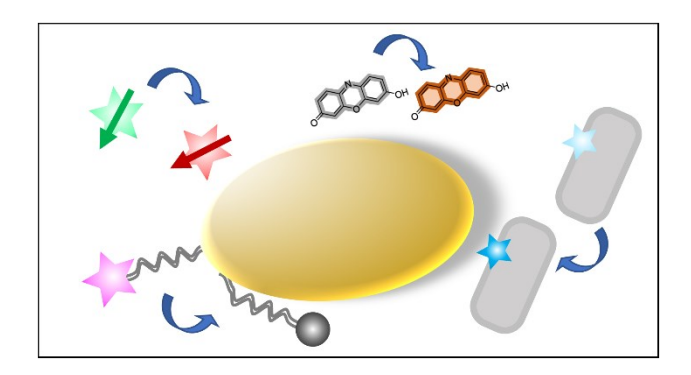
Saaj Chattopadhyay¹ and Julie S. Biteen**,2

¹Applied Physics Program, University of Michigan, Ann Arbor, MI 48109

²Department of Chemistry, University of Michigan, Ann Arbor, MI 48109

*Correspondence to: <u>jsbiteen@umich.edu</u>

TOC Graphic.



Introduction

Since the seventeenth century when the earliest microscopes explored the vibrant microbial communities in the blood and in pond scum¹, microscopists have innovated to visualize new structures and processes. Though light microscopes were limited by the wavelength of light for hundreds of years, super-resolution microscopy techniques now enable the study of nanometer-scale structures and processes^{2–4}. These nanoscopic characterization tools have had great impact for understanding subcellular biology and organic materials⁵. Increasingly, super-resolution microscopy is being applied to measure the light-matter interactions between fluorescent dyes and plasmonic metal nanoparticles (NPs). These near-field interactions occur on the few nanometers scale that super-resolution microscopy is ideally suited to investigate⁶. Furthermore, super-resolution microscopy can detect the effects due to plasmonic coupling on the emissive properties—brightness, polarization, and spectrum—of nearby dyes, and can characterize heterogenous distributions. Overall, super-resolution microscopy can recognize subtle changes to address fundamental questions about fluorescence^{7–12} and applied questions such as catalysis and ligand arrangement^{13–16}. This review describes recent progress using single-molecule super-resolution approaches to understand plasmon-coupled fluorescence.

Single-Molecule Super-Resolution Microscopy

Super-resolution microscopy beats the ~0.5 μm standard diffraction limit of light ^{17–20}. Approaches based on single-molecule localization have had particular impact in uncovering the nanometer-scale fundamentals of plasmon-coupled fluorescence because this non-invasive approach can directly measure the effect of a metal NP on proximal dyes in a conventional epifluorescence microscope. The core innovation in single-molecule fluorescence microscopy is straightforward: when a fluorescent molecule (fluorophore) is in a homogeneous environment, a fit to the diffraction-limited image of a single fluorophore indicates the fluorophore position with a localization precision much better that the standard diffraction limit (Figure 1a,b)²¹. Single molecules can therefore be localized to within a few nanometers while maintaining the advantages of benchtop fluorescence microscopy, which directly characterizes light-matter interactions *in situ*. In addition to determining the brightness and the two- or three-dimensional position of each dye molecule, single-molecule microscopes can be extended, for instance to measure the fluorescence polarization^{6,10}, spectrum¹¹, and lifetime¹².

This sub-diffraction localization is however only possible when the fluorophores being detected are isolated in time and space such that the image of the isolated dye molecule depicts the microscope point spread function (PSF), which is defined as the response of the microscope to a point source. Fortunately, a toolbox of super-resolution methods has emerged to map the fluorescence of a dense collection of molecules, for instance to image a collection of dyes interacting with a metal NP²⁻⁴. These methods all achieve super-resolution images by detecting and localizing one molecule at a time, though each method realizes this temporal separation in a different way. For instance stochastic optical reconstruction microscopy (STORM)² and photoactivated localization microscopy (PALM)^{3,22} achieve super-resolution images by using labels that can be made fluorescent (photoactivated or photoswitched) by high-frequency illumination; in each imaging cycle, only a sparse subset of labels are photoactivated and subsequently imaged and localized until the dyes become dark (non-absorbing) and then the cycle of photoactivation and imaging is repeated. Direct STORM (dSTORM) and ground state depletion with individual molecule return (GSDIM) are like PALM and STORM, but instead of using a second laser for photoactivation, GSDIM and dSTORM image dye molecules that stochastically blink under illumination in the imaging conditions^{4,23}. Points accumulation imaging in nanoscale topography (PAINT) achieves sparse single-molecule images by imaging dye molecules as they are transiently immobilized by adsorption onto a surface²⁴. Each molecule is imaged and localized until it photobleaches or desorbs. In this scheme, free molecules are not detected, either because their fluorescence is dim until rigidification on the surface or because freely diffusing molecules are blurry on the imaging timescale (typically tens of ms). DNA-PAINT adds specificity to the PAINT imaging scheme: rather than rely on dye adsorption at random positions on the sample, DNA oligonucleotides labeled with a dye molecule bind reversibly to complementary DNA docking strands²⁵. All of these methods separate the fluorophore imaging in time to achieve single-molecule localizations at low densities by optimizing the dye concentration, laser power, and imaging frame times.

Plasmon-Enhanced Fluorescence

In single-molecule localization, the uncertainty on the fit of a fluorescence image scales inversely with the square root of the number of photons collected²¹. Thus, since the superresolution methods described above rely on localizing a series of single dye molecules, the

resolution improves as the number of photons collected per fluorophore increases. Plasmonic NPs can enhance the fluorescence of nearby fluorescent emitters^{26–28} and promise to increase the resolution of single-molecule microscopy. A plasmon mode is a collective oscillation of the electron cloud bound in a material²⁹. Noble metals support strong plasmon modes because of their low absorption losses. At the interface between a metal and a dielectric, surface plasmon polaritons are created by incident electromagnetic waves, and this plasmon mode can travel on the metal surface. When this propagation length is physically restricted, i.e., in metal NPs with dimensions smaller than the wavelength of light, the surface plasmon polariton is localized²⁹. This localized surface plasmon resonance (LSPR) oscillates within the NP at a resonance frequency that depends on the materials properties of the metal and its surroundings, as well as on the NP size and shape. Because the plasmonic NP interacts strongly with incident illumination, these LSPRs give rise to plasmon-enhanced spectroscopies including plasmonenhanced fluorescence^{30–32}. There are two main pathways for this enhancement: (1) The NP concentrates the field of incident illumination to enhance the absorbance cross section of a nearby dye, and (2) the NP increases the local density of photonic states (LDOS) in its vicinity to increase the radiative rate of a nearby excited dye²⁹.

Fluorescence Reshaping

Single-molecule microscopy has revealed that the emission patterns of fluorescent molecules are altered in the presence of a plasmonic NP (Figure 1c)^{7,8,33–37}. Whereas single-molecule localization relies on finding the center of the emission pattern of an fluorescent molecule in an isotropic medium²¹, this coupled emission pattern shows that the significant spatial variance in the local electromagnetic field around a NP creates distortions: the image of a single fluorescent molecule near a plasmonic NP is not an accurate indication of the microscope PSF. As a result, the center of the image of a fluorescent molecule coupled to a plasmonic NP does not necessarily indicate the actual molecule position^{7,8,33–37}, and plasmon-enhanced fluorescence is therefore not a straightforward way to increase single-molecule imaging resolution.

Fortunately, the mislocalization between the ground truth molecule position and the apparent image position can be understood computationally^{7,8,33} and analytically^{6,10}. Furthermore, experimental data can provide a lookup table to correct the artifacts in plasmon-coupled images^{7,8} and analytical models are being developed to provide fit functions that return the true

molecular position instead of the center of the emission pattern⁶. These models will be greatly improved when all the effects of plasmonic NPs on nearby molecules are characterized. For instance, in addition to measuring the brightness and apparent position of plasmon-coupled fluorescent molecules, single-molecule spectroscopy has measured changes in the dye emission spectrum¹¹ and polarization-resolved single-molecule imaging has characterized changes in the apparent molecular orientation¹⁰. Thus, the imaging artifact can be turned into a detection scheme for a variety of applications. The increasing ease in fabrication techniques, and a wide variety of fluorophores, offers an exciting range of potential applications in biological and chemical sensing^{38–40}.

Applications of Super-Resolution Imaging to Nanoparticle Plasmonics

In addition to fluorescence, plasmonic NPs affect other behaviors due to their ability to concentrate electric field in their local environment. The large surface area offered by plasmonic NPs also makes them chemically active substrates for high-throughput experiments. Thus, mapping and understanding the heterogeneity of light-matter interaction in the vicinity of a plasmonic NP has been a rich field of study^{12,13,34,41,42}. Near-field imaging techniques like nearfield scanning optical microscopy (NSOM) and cathodoluminescence can directly map the electric field about a plasmonic NP⁴³⁻⁴⁵, but these probes distort the electric field that they measure⁴⁶. Thus, building tools that read out this information without perturbing the system is crucial to engineer devices that employ plasmonic nanoantennas 39,41,47,48. Furthermore, far-field techniques like optical microscopy directly investigate light-matter interactions by measuring the response of a dye molecule to its environment³⁴ and super-resolution microscopy measures the heterogeneous spatial response of plasmon-coupled fluorescence in the vicinity of plasmonic NPs to directly probe the near-field dye-NP interaction⁴⁹. Recent super-resolution investigations have also recorded and understood the correlation between the response of the dye-NP interaction and the local electric field ^{12,13,34,41,42}. Therefore, single-molecule fluorescence imaging offers the flexibility to experimentally study the nanoscale environment and topography as well as the effect of a NP on nearby dye molecules while still providing nanometer-scale resolution.

Mislocalization of the Molecular Emitter

Coupling dye molecules to plasmonic NPs increases the precision of the single-molecule localization by enhancing fluorescence to decrease the error on the mean position²¹. However, a shift between the position of the detected signal and the actual position (ground truth position) of the emitter decreases the accuracy of the plasmon-coupled measurement (Figure 1b,c). Thus, quantifying this shift is crucial to enable plasmon-enhanced super-resolution microscopy. To measure the mislocalization of a fluorophore in the presence of a plasmonic NP, the ground truth position must be known for comparison.

Fu et al.⁸ characterized the mislocalization of single molecules by plasmonic NPs with a highly symmetric sample system that encodes *a priori* knowledge of the dye-NP separation distance. The assembly is composed of dye molecules attached covalently via rigid double-stranded DNA spacers to the surface of a spherical gold NP (Figure 2a). Here, the relative distance between the NP and the dye is defined by the number of DNA base pairs, and thus the apparent position can be compared to the actual position. Single dye molecules were detected with dSTORM imaging (Figure 2b)²³. Though all NP-dye separation distances are the same in this geometry, the ability to accurately localize the dye molecule is compromised by three separate effects. In addition to (1) the shift between the actual position and the apparent position due to the presence of a plasmonic NP, the authors consider that (2) though all the molecules are equidistant in 3D from the NP, the axial position is lost when a 3D system is imaged in a 2D microscope, and (3) the localization precision is finite ($\sim 10 - 20$ nm) in these photon-limited experiments.

To select dye molecules only around the xy plane periphery of a 179-nm NP, the authors used a 3D microscope. Based on the astigmatism produced by a cylindrical lens, the z-position of the NPs and the dye molecules were resolved to \pm 60 nm (Figure 2c)^{50,51}. Based on these 3D coordinates, the authors optically sectioned the center ring of the NP (Blue square in Figure 2c; Figure 2d). The optical sectioning yielded a 2D symmetric NP-dye assembly. On the other hand, since larger NPs provide only subtle fluorescence enhancements, Fu et al. also studied smaller (78.6 nm diameter) NPs, which provide a stronger fluorescence enhancement⁵². However, these NPs could not be optically sectioned into a disc with the 3D microscope's z-resolution. To account for the 2D geometry in these smaller assemblies, Fu et al. therefore compared the peak

positions of the single-molecule detections to simulated data for an ideal dSTORM experiment in this geometry. The 2D projections of the simulated system and the experimental image were then compared to determine the mislocalization.

The third imaging limitation, that of photon-limited detections, could not be explicitly removed, but was accounted for in simulations as well. Overall, the experimental results were qualitatively comparable to the results from full-field electromagnetic (finite difference time domain; FDTD) simulations, and the study concluded that the emission pattern is mislocalized toward the center of mass of the coupled dye-NP system: the apparent position of the dye is closer to the NP than the actual position of the NP (yellow focus vs. red line in Figure 2e)^{37,53–57}. This mislocalization depends strongly on the separation distance (Figure 2f). Although the authors did not arrive at an analytical relationship between separation distance and mislocalization, the results provide a reference for future work with Au NPs.

Raab et al.⁷ further examined this mislocalization effect by engineering two systems with *a priori* knowledge of the relative positions of the NP and the dye molecule. The first system is composed of a 12-helix bundle DNA origami structure with three DNA-PAINT marks placed 80 nm apart (Figure 3a). The DNA-PAINT marks are specific sites where complementary dyes transiently bind, fluoresce, and unbind, to produce single-molecule fluorescence events²⁵. In addition to these three dye-binding sites, the structure has a single docking site for a DNA-modified Au NP (Figure 3b)⁵⁸. The helix bundle provides a rigid backbone that ensures no physical distortion in the system and the DNA structure dictates the precise locations of the marks and docking sites⁵⁹. In the absence of NPs, the DNA-PAINT experiment registers the actual positions of the DNA-PAINT marks: three spots in a straight line separated by 80 nm (Figure 3a). When NPs are introduced to the PAINT experiment and a NP docks onto the bundle, the center fluorescent signal is displaced from the reference line and the three dyes instead appear as a triangle (Figure 3b). This result provides qualitative evidence of mislocalization.

To quantitatively analyze the so-called "single-molecule mirage," Raab et al. built a second system. The second system includes two structures: the reference structure and the sample structure. The reference structure is a DNA origami plane with DNA-PAINT marks arranged 50 nm apart in an equilateral triangle (Figure 3c). The sample structure is a single DNA-PAINT mark and a docking site for DNA-modified Au NP; NP-induced mislocalization produces a

deviation in the emission pattern of the sample structure relative to the reference pattern (Figure 3d). To record the shift, the deviation measured in these images was calibrated to the plane of the reference structure and the shift is the difference between the average fluorophore position with and without the NP (Figure 3e).

The authors observed the shifts as a function of NP size (20 – 80 nm diameter). By using astigmatism through a cylindrical lens^{50,51}, and by localizing ~10,000 molecules per NP, the authors observed that the PSF is shifted toward the center of the NP for all NP sizes, consistent with previous experiments^{37,53–57}, and that this shift increases with the NP diameter (Figure 3f). This trend, which is expected because the strength of the LSPR mode of a NP increases with diameter⁵², is also found in numerical simulations, though the experimental shift is even larger than the calculated shift, especially for the larger NPs. This discrepancy is attributed to changes in the optical properties of the local environment due to high DNA concentrations⁶⁰. Although the authors did not arrive at an analytical relationship between separation distance and mislocalization, the experiments point to a rigorous engineering solution to measuring mislocalization effects. Consistent with prior studies, additional FDTD calculations predicted that the separation distance between the molecular emitter and the NP and the excitation frequency of the laser will affect the mislocalization as well^{34,56}.

Overall, the two studies point to a very important problem in implementing plasmon-enhanced single-molecule super-resolution microscopy: localization-based super-resolution imaging affords a precision of about 20 nm and this precision can be improved by using plasmonic NPs to enhance the dye brightness, but the plasmon-coupled fluorescence suffers from an average mislocalization greater than the localization precision. For instance, in Raab et al.⁷, the average mislocalization of a dye 10 nm away from an 80 nm Au sphere is 29.2 nm. Mislocalization at this scale would obfuscate any information gained from plasmon enhancement. Moreover, though Raab et al. found a distinct shift in the PSF position, they recorded no measurable distortion in the PSF shape. This result is surprising because previous experiments have shown that the asymmetry of the fluorophore-NP system skews the PSF toward the NP^{35,37,61,62}. Thus, this work indicates that there is not always a clear indicator that mislocalization has occurred.

Spectral Reshaping of the Molecular Emitter

In addition to producing a shift in position, a plasmonic NP can change the emission spectrum of a nearby dye⁶³. Spectral shifts of coupled NPs have been used in the past as plasmonic rulers to measure separation distances, and hyperspectral plasmonic-coupling microscopy^{64,65} extends this approach to precisely monitor clustering of proteins⁶⁶. By implementing single-molecule hyperspectral imaging, Lee and Biteen recorded changes in the emission spectra of single dye molecules near Au NPs. The study considered four dyes with different peak fluorescence emission wavelengths ranging from 510 to 610 nm. Each dye therefore had a different spectral overlap with the NP, which has an LSPR peak at 575 nm (Figure 4a). Combining PAINT as the super-resolution imaging technique with single-molecule spectroscopy, they determined the position and emission spectrum of each molecule detected²⁴. Because plasmon coupling is distance-dependent, the single-molecule approach permitted differentiation between molecules close to the NPs and molecules too far away for significant coupling to occur. Indeed, consistent with FDTD simulations, the hyperspectral microscopy results indicated that, for all four dyes chosen, the emission spectra of dye molecules more than 40 nm from the NPs are not significantly different from the intrinsic spectrum of the uncoupled dyes (Figure 4b).

On the other hand, the hyperspectral single-molecule microscopy revealed important spectral changes at the smallest separation distances, especially for the dyes with emission peaks most detuned from the LSPR maximum (Figure 4b). For the bluest dye, BDP-FL, a red shoulder appears (red arrows in Figure 4c); these experimental observations are supported by calculations (Figure 4c). This observation of wavelength-dependent plasmon-coupled fluorescence emission from single molecules indicates that plasmon enhancement is a resonant effect that can select specific radiative transitions in a dye molecule. Beyond uncovering these basic physical principles, one important consequence of this work is that because the spectral reshaping depends on the LSPR frequency of the NP, the spectral shift can be used to differentiate between different NPs. This detection scheme holds promise as the basis for high specificity sensors to discern heterogeneities in plasmonic NPs.

Apparent Rotation of the Emitter Polarization

In addition to affecting the position and the emission spectrum of the fluorophore, the polarization of the coupled fluorescence emission is altered in the presence of a NP. Goldwyn et al. 6 considered the coupled system of a plasmonic NP and a fluorophore in analogy with Young's double slit experiment. This classical interpretation of light interacting with two slits yields a scattering pattern that is the result of constructive and destructive interference of the scattered light from the individual slits (Figure 5a). Because a slit is theoretically equivalent to an electric dipole with direction and magnitude given by the orientation and width of the slit, Goldwyn et al. proposed an analytical model for plasmon-coupled fluorescence that treats both dye molecules and NP LSPR modes as dipoles⁶. The dipole orientation and magnitude of the dye depend on the electronic structure and quantum efficiency of the dye, and the plasmonic mode orientation and magnitude depend on the NP size and structure. While electrodynamic effects can be computed by solving Maxwell's equations numerically, the underlying physics are not explicitly revealed. For instance, several dipole and higher-order modes contribute to dye-NP coupling. By modeling the NP and the dye molecule as a pair of dipoles with associated magnitude and direction, as well as the polarization of incident light, the model can explain changes in the emission pattern upon dye-NP coupling.

Zuo et al.¹⁰ expanded this theoretical framework with experimental data for the apparent orientation of dyes in the presence of a plasmonic NP. Nanorods (NRs) acted as asymmetric plasmonic NPs with a defined LSPR orientation: the longitudinal plasmon mode is aligned along the NR long axis. PAINT measurements captured the fluorescence images of single dye molecules as they transiently adsorbed on the surface near the NRs²⁴. The NR orientation as well as the apparent emission dipole orientation of each dye molecule were measured with polarization-resolved single-molecule microscopy: a polarizing beam displacer in the emission pathway separated the emission into two orthogonally polarized outputs and the ratio of the intensities in these two channels indicates the dipole orientation. PAINT measurements of dye molecules transiently adsorbing on the microscope coverslip in the absence of Au NRs (Figure 5b) indicate that the dyes are randomly oriented on the surface; an experimental bias toward the center (45°) is attributed to *z*-oriented molecules as well as low signal-to-noise artifacts. On the other hand, red Cy5.5 dyes that are coupled to Au NRs appear to be rotated toward the NR long

axis (black arrows in Figure 5c,d); this rotation was observed for all angles: the apparent molecule angle generally indicates the NR angle (Figure 5e). Moreover, some subtle plasmon-induced emission polarization rotation was even observed for the bluer Cy3 dye molecules that are far detuned from the Au NR LSPR peak.

To understand this apparent rotation in the emission pattern, the authors expanded the theoretical framework⁶ to include the NR geometry, which was approximated as a prolate spheroid. This extended analytical model includes all the dominant electrodynamics of the system as indicated by its ability to predict both the apparent mislocalization and the apparent rotation of the dye consistently with FDTD simulations¹⁰. By explicitly considering all the underlying physics, the analytical model explains the origin of the polarization rotation effects. As the emission intensity is the square of electric field, the emission pattern is not a simple superposition of two coupled systems. The resulting interferences are important, and their effect is uncovered in this investigation (pink box in Figure 5f, Figure 5g). Furthermore, though the NR has a dominant longitudinal mode that is resonant with Cy5.5 emission, plasmon resonances along the weaker, blue-shifted transverse mode play a role as well. Overall, in addition to using single-molecule polarization-sensitive microscopy to detect plasmon-coupled fluorescence rotation, Zuo et al. provided insight into plasmon modes, their relative strengths, and where and how interference effects are introduced in the system.

Mapping Light-Matter Interactions near a Plasmonic Nanoparticle

Characterization of the emission pattern is not only a key step in utilizing plasmonics to enhance fluorescent signals for super-resolution microscopy, it is also a crucial step toward utilizing plasmonics to control light-matter interactions. Plasmonic NPs can enhance fluorescence by concentrating the incident light to increase absorption and by more efficiently re-radiating the dye emission from the near-field to the far-field due to an increased local density of photonic states (LDOS). Previously, Wertz et al. coupled dyes to Au nanotriangles and found that although plasmonic coupling at the excitation wavelength to increase the absorption is a critical component of the fluorescence enhancement, the emission pattern mislocalizations can be reproduced mainly by considering only plasmonic coupling at the emission wavelength⁵⁶. Mack et al.⁹ decoupled these two pathways by comparing how Pacific Orange (PO) and Pacific Blue (PB) couple to plasmonic nanoantennas. Importantly, these two dyes have similar absorbance

spectra (dashed lines in Figure 6a), but PO has a large Stokes shift, and therefore a redder fluorescence emission spectrum than PB (dashed lines in Figure 6b). The PO and PB were coupled to plasmonic aluminum tri-disk nanoantennas with a peak LSPR frequency that matches the absorbance maxima of both dyes (Figure 6a); this LSPR frequency is also resonant with the PB emission spectrum (Figure 6b).

When the samples are excited at 405 nm, the tri-disk nanoantenna concentrates the electric field at hot spots between the Al disks; absorbance enhancement should be maximized for molecules at these hot spots. The tri-disk arrangement produces an electric field that depends on the polarization of the excitation beam (Figure 6c,d). Thus, when enhanced excitation is the predominant coupling effect, the emission pattern should depend strongly on the excitation polarization, whereas dye molecules that also benefit from coupled emission will see a less pronounced polarization dependence. Accordingly, the PAINT super-resolution localization maps for the PB dye are insensitive to the excitation polarization (Figure 6c), consistent with the PB excitation and emission wavelengths both being resonantly coupled to the nanoantenna wavelength. On the other hand, the PAINT super-resolution localization maps for the PO dye varies strongly with excitation polarization (Figure 6d), consistent with the fact that the excitation enhancement dominates while the PO emission is strongly detuned from the LSPR.

The electric field about NPs has been discerned by mapping single molecules at random positions around the NP^{9–11,49}. However, as discussed above, mislocalization in the superresolution image leads to an inaccurate representation of the electric field map. It is therefore desirable to control the fabrication processes of plasmonic systems to probe the electric field at well-defined positions of precisely placed molecular emitters³⁸. This positioning is challenging, and even when realized as in studies like those of Raab et al. and Fu et al.^{7,8}, the positioning is static (Figures 2 and 3). In contrast, Xin et al.¹² designed and studied a dynamic system based on DNA origami in which the dye-NP separation varies with time as the dye moves toward the hotspot of an Au nanosphere dimer (Figure 7a). At the hotspot, this dimer concentrates an intense electric field (Figure 7b)^{67–69}.

The dynamic system was created with DNA origami by placing a track with nine footholds (complementary DNA stators attached to the track bundle) at known positions along the plane between two Au nanospheres. A fluorophore attached to a DNAzyme strand thus becomes an

autonomous walker. Upon the introduction of a trigger DNA strand and divalent metal ions, the walker progresses unidirectionally along the footholds and into the hotspot using a burnt-bridge mechanism. As the fluorophore walked toward the hotspot, the fluorescence intensity (Figure 7c) and lifetime (Figure 7d) were recorded at each foothold position. The fluorescence lifetime decreases, and the fluorescence intensity increases as the molecule approaches the hotspot.

The authors additionally considered that while the dye orientation plays a factor for enhancement—for instance, in this geometry a dye oriented in the x or z direction would experience less enhancement than one oriented in the y direction⁷⁰—the strand attached to the dye allows it to freely rotate at a time scale shorter than the fluorescence lifetime⁷¹. Thus, averaged over the image integration time, each molecule was considered as an isotropic emitter. Overall, this powerful DNA origami design could be applied to different NP-dye pairs to create tunable devices in which the coupling between the dye and the molecule can be adjusted in real time. It will be exciting to see this approach combined with current innovations in DNA origami to take advantage of increasingly robust and rigid designs and to study systems in which reversible actuators can precisely modulate both the position and the orientation of molecules.

Applications of Single-Molecule Microscopy in Plasmonics

When NPs are be employed as sensors and devices, their surfaces are often functionalized with organic ligands or DNA spacers^{72–74}. Understanding the behavior and distribution of ligands covalently bound to metals is an important step in utilizing plasmonics in these systems^{75–77}. Cheng et al.¹⁴ compared the effects of plasmon-mediated photothermal heating and direct heating on ligand organization. They visualized double-stranded DNA (dsDNA) ligands bound to a Au nanorod (NR) by attaching a 5-carboxytetramethylrhodamine (TAMRA) fluorophore to the far end of each ligand. Based on the GSDIM single-molecule imaging approach in which the TAMRA dye is switched between the non-emissive triplet state and its fluorescent singlet state under laser excitation, sparse subsets of single molecules were imaged to provide a superresolution image of the TAMRA dye positions^{4,78}. In this experiment, mislocalization was avoided by decoupling the dye and LSPR wavelengths, and additionally, because fluorescence is quenched when a dye and a metal NP are in contact^{79,80}, this study differentiated between dark collapsed ligands and bright upright ligands (Figure 8a).

Normally, immobilized TAMRA dye molecules exhibit strong bursts of fluorescence activity upon laser excitation. However, no fluorescence was observed at the start of illumination of the NP-ligand-dye samples. Rather, the bursts increased in frequency and intensity over time (Figure 8a). These observations indicate that initially, ligands are in a collapsed arrangement where the fluorophores are very close to the surface of the NP (< 5 nm) and thus, fluorescence is quenched, then the ligands slowly rearrange into an upright arrangement such that the fluorescence can be recovered. Interestingly, the experiment indicates that the upright arrangement of the ligands is triggered by heat, as it could alternatively be produced with preheating to 40 °C. The time evolution of the laser-induced heating was measured (Figure 8b) and the study found that the plasmon-mediated photothermal heating produced nearly the same extent of ligand reorganization as the 40 °C thermal treatment. Furthermore, through their single-molecule approach, Cheng et al. mapped heterogeneity of ligand binding. More fluorescence events were observed at the NR ends than at the middle, and this heterogeneity was more significant for the plasmon-mediated heating than for the pre-heated samples. This result is consistent with a spatially dependent thermal profile. Overall, this study indicates that plasmon-mediated photothermal heating can trigger ligand rearrangement and could be used to control interactions in the near field of the NP.

In addition to interacting with ligands, metals surfaces catalyze a wide variety of chemical reactions and metal NPs greatly increase the surface area offered for catalysis^{81–87}. Plasmonic NPs can also concentrate the incident light to small volumes increase reactivity. In addition, hot electrons produced at the NP surface catalyze reactions because they provide electrons for intermediate reaction steps^{86–91}. Thus, the electric field hotspots in plasmonic NPs serve as catalytic hotspots. Zou et al.¹³ studied catalytic hotspots on linked Au NR dimers using correlative super-resolution imaging and electron microscopy. Pairs of NRs were joined with biotin-streptavidin linkages, and the dimer was coated with a layer of mesoporous silica to stabilize the structure and avoid aggregation while still providing reactants access to the metal surface for catalysis via the pores^{92,93}.

Single-molecule microscopy visualized the conversion of fluorogenic resazurin reactants into the fluorescent resorufin product. Every time a resorufin molecule desorbed from the metal surface and slowly traversed the mesoporous silica shell, a single molecule was detected. In addition to measuring the product formation rate, the single-molecule fluorescence approach

enabled the authors to spatially resolve the reactivity: the number of localization events is proportional to the amount of product formation (Figure 8c). Thus, this study identified nanometer-scale catalytic hotspots on the NR dimers, and correlated these optical microscopy measurements with electron microscopy to conclude that these systems had high catalytic rates at the nanoscale gaps between the NRs (Figure 8d), where an intense electric field hotspot is predicted by FDTD simulations. This work extends super-resolution imaging to measurements of chemical reactivity.

Interactions of Molecules with Plasmonic Nanoarrays

Beyond single-particle measurements, arrays of NPs can be used as a high-throughput substrate for imaging many single-particle events. Hamans et al. ¹⁵ studied the nanometer-scale patterning of the emission enhancement over a plasmonic array to differentiate between the contributions from the LSPR of each NPs and the SLR (surface lattice resonances) of the array. An SLR mode arises in plasmonic arrays due to the coupling of confined oscillations of the electric field within the array ^{94,95}. The boundary conditions for these oscillations are the surfaces of neighboring NPs. In contrast, each individual NP has an LSPR mode due to the confined oscillations of the electric field within the NP. The boundary condition for these oscillations is the surface contour of that NP. Thus, Hamans et al. engineered a hexagonal array of truncated Al cones (Figure 9a,b) to have a broad LSPR peak that is red-shifted relative to the dye (Figure 9c) and a sharp SLR peak that overlaps with the emission spectrum of the dye (Figure 9d). The spacing between the cones determines the strength and the wavelength of the SLR ^{95,96}. Computations indicate that the electric field at the LSPR wavelength is localized around the base of the NPs (Figure 9e), whereas the electric field is more diffuse at the SLR wavelength (Figure 9f).

The authors used PALM microscopy to map the fluorescence pattern of caged dyes embedded in a polymer layer. They imaged two samples: (1) with the polymer layer at the base of the array, to study enhancement due to the LSPR (Figure 9a), and (2) with the polymer layer 100 nm above the array, to study enhancement due to the SLR (Figure 9b). The presence of plasmonic NPs affects the absorption cross section of the dye, the spontaneous decay rate, and the direction of the emission²⁹. Here, the absorption enhancement is minimal because there is minimal array extinction at the excitation laser wavelength (532 nm). By sectioning the spectra

using emission filters (Figures 9c,d), the study recorded only enhancement due to each respective resonance mode: LSPR or SLR. Simulations of the electric field intensity about a truncated Al cone at the LSPR wavelength predicted a strong field enhancement at the NP surface near its base (Figure 9e) while simulations at the SLR wavelength predicted fields that extend farther into the surrounding medium. Thus molecules in the plane at the array base (Figure 9a) were predicted to couple to the LSPR and molecules in the plane above the array (Figure 9b) were predicted to couple to the SLR. For the LSPR-coupled fluorescence, the study found enhanced fluorescence intensity, and the most enhanced molecules appeared to be at the NP position (center of pattern in Figure 9g). For the SLR-coupled fluorescence, the emission pattern was uniform, and the fluorescence intensity was not enhanced relative to an isolated dye (Figure 9h). The study concluded that the LSPR plays the dominant role in fluorescence enhancement and that strong mislocalization occurs upon LSPR-coupled emission. On the other hand, the SLR mode of this structure is still coupled: FDTD simulations indicate that coupling to the SLR mode can control the directionality of the emission. Overall, this work concludes that the LSPR mode is dominant over the SLR mode of larger scale arrays, in which case, the NP array can be simply considered as an ordered collection of single plasmonic antennas.

Stephen Lee et al. used such plasmonic arrays to increase fluorescence intensities in live-cell single-molecule fluorescence imaging and to explore the number of variables that can be modified to optimize plasmon-enhanced single-molecule imaging¹⁶. While plasmon-enhanced fluorescence has been extensively studied⁴⁹, it has not been widely applied to live-cell superresolution imaging. Au nanotriangle arrays were fabricated on a microscope cover slip by nanosphere lithography^{97,98}. Polystyrene beads were self-assembled into a mask to template an array of Au nanotriangles. Because the spaces between close-packed spheres form equilateral triangles, changing the sphere diameters tunes the triangle size and the spacing between the triangles. Because the evaporated Au thickness was constant, the LSPR peak wavelength of each nanotriangle scaled with its edge length. Nanosphere lithography is a relatively straightforward scheme to fabricate extensive arrays of plasmonic NPs, but it does not afford independent control over the fabrication parameters: larger triangles are spaced farther apart and smaller triangles are more densely packed. Three different sizes of nanotriangle arrays were prepared from polystyrene beads with diameters of 500-1000 nm (Figure 10a – c), and several trends were measured by dark-field scattering spectroscopy: (1) the largest NPs had the highest scattering

cross sections, (2) the smallest NPs had the highest spectral overlap with the red fluorescent protein PAmCherry under investigation, and (3) the smallest NPs were more densely packed on the coverslip. All of the nanotriangles were spaced far enough to avoid the significant SLR modes discussed above¹⁵.

Membrane proteins play an important biological role and are well positioned for coupling to extracellular plasmonic NPs: plasmon-enhanced fluorescence is a near-field effect, and the membrane is about 20 nm thick. By studying the emission intensities of single fluorescent proteins in the membrane of cells above different nanotriangle arrays, this paper sought to find the optimal plasmonic substrate. The proteins TcpP and ToxR in the Vibrio cholerae membrane are crucial regulators of the expression of the deadly cholera toxin. TcpP and ToxR were genetically tagged with two photoactivatable fluorescent proteins: the red PAmCherry and the green PAGFP, respectively. Single-molecule measurements of these fluorescent labels in living V. cholerae cells prepared on top of Au nanotriangle arrays indicated that the fluorescence enhancement was higher for TcpP-PAmCherry than for ToxR-PAGFP: the TcpP-PAmCherry brightness was increased more than 2-fold whereas the ToxR-PAGFP brightness had a more modest 1.2× enhancement. Furthermore, the fluorescence enhancement varied with substrate geometry: the average TcpP-PAmCherry molecule brightness increased the most (2.1×) upon coupling to the smallest NPs (Figure 10d), presumably due to their high surface coverage: the detected molecules were more likely to be in the near field of one of these densely packed NPs. The fluorescence enhancement was still significant (1.6×) for the largest NPs (Figure 10f): even though the surface coverage decreases, each NPs has a significantly larger scattering cross section. In fact, the enhancement was smallest for the intermediate NPs, for which the spectral overlap was weak while the surface density was also low (Figure 10e). Thus, for similar live-cell imaging in the future, though these nanotriangle arrays are a low-cost solution to producing high coverage, non-toxic plasmonic substrates, their geometry is not ideal. Plasmonic arrays should be designed maximal surface coverage, maximal NP scattering cross sections, and maximal spectral overlap with the fluorescent probe.

Conclusions

In conclusion, recent work has quantified light-matter interactions near plasmonic NPs. NPs produce novel environments at the nanoscale by concentrating far-field illumination and super-

resolution microscopy can characterize how fluorescence is affected by this modified environment. Simulations of the electric field around the NP predict the energy landscape, but these simulations do not identify the underlying physical principles that contribute to plasmon-coupled fluorescence—for instance, the contributions of orthogonal dipole modes and interference terms. Rather, the work reviewed here uses super-resolution fluorescence microscopy to characterize the local response of a dye to a single plasmonic NP in order to provide physical insight about how this NP gives rise to changes in dye emissivity and chemical activity near its surface.

Going forward, it would be exciting to study new variables in single-molecule/single-particle interactions. For example, the effect of the chirality of both the NPs and the fluorophores could be explored with different polarizations of light. Furthermore, the engineering solutions demonstrated in this Review show that the field is moving toward experimental geometries that provide increased certainty about dye positioning and dye-NP separation, as well as toward microscopy approaches that yield increased knowledge about the emission. The reviewed studies all indicate that molecules respond heterogeneously to NPs depending on their specific local environments, and further work is needed to uncover these nanoscopic gradients. In addition to enhancing fluorescence, metal NPs augment other plasmon-mediated phenomena such as photothermal heating and catalysis. If the nanometer-scale coupling between dyes and NPs can be understood, NPs will be hugely advantageous for designing devices with increased sensitivity and specificity. The programmability of these sensors and devices increases with the ease of nanofabrication of novel plasmonic systems.

Author Biographies

Saaj Chattopadhyay

Saaj Chattopadhyay received her B.S. in Engineering Physics from Cornell University in 2019. Her undergraduate research involved developing correlative light and electron microscopy techniques for studies at cryogenic temperatures and characterizing the exfoliation of 2D materials as a sample preparation technique for transmission electron microscopy. Through this work, she developed an interest in interdisciplinary approaches to study the microscopic world. Her Ph.D. research in the Biteen Lab at the University of Michigan focuses on the interactions

between plasmonic nanoparticles and polarized light. In addition, she has an active interest in science education and research-based instructional strategies.

Julie Biteen

Julie Biteen is an Associate Professor of Chemistry at the University of Michigan, where her research program develops super-resolution fluorescence microscopy for applications to nanomaterials and microbiology. Dr. Biteen earned an M.S. in Applied Physics and a Ph.D. in Chemistry at California Institute of Technology where she studied plasmon-enhanced luminescence. Dr. Biteen trained as a postdoc at Stanford University, studying structural proteins in living bacteria cells with single-molecule imaging and super-resolution microscopy. The Biteen Lab combines these areas to uncover nanometer-scale fundamentals of cell biology and plasmonics. Dr. Biteen's contributions have been recognized by numerous awards, including the Margaret Oakley Dayhoff Award for Women in Biophysical Sciences (2017), the Journal of Physical Chemistry Award Lectureship (2016), a Burroughs Wellcome Fund Career Award at the Scientific Interface (2009), and an NSF CAREER Award (2013).

Acknowledgements

We thank Shelby Nicolau and Zechariah Pfaffenberger for their critical reviews of the manuscript. We appreciate support from National Science Foundation (award CHE-1807676).

References

- (1) Porter, J. R. Antony van Leeuwenhoek: Tercentenary of His Discovery of Bacteria. *Bacteriol Rev* **1976**, *40* (2), 260–269.
- (2) Rust, M. J.; Bates, M.; Zhuang, X. Sub-Diffraction-Limit Imaging by Stochastic Optical Reconstruction Microscopy (STORM). *Nature Methods* **2006**, *3* (10), 793–796. https://doi.org/10.1038/nmeth929.
- (3) Betzig, E.; Patterson, G. H.; Sougrat, R.; Lindwasser, O. W.; Olenych, S.; Bonifacino, J. S.; Davidson, M. W.; Lippincott-Schwartz, J.; Hess, H. F. Imaging Intracellular Fluorescent Proteins at Nanometer Resolution. *Science* **2006**, *313* (5793), 1642–1645. https://doi.org/10.1126/science.1127344.
- (4) Fölling, J.; Bossi, M.; Bock, H.; Medda, R.; Wurm, C. A.; Hein, B.; Jakobs, S.; Eggeling, C.; Hell, S. W. Fluorescence Nanoscopy by Ground-State Depletion and Single-Molecule Return. *Nature Methods* **2008**, *5* (11), 943–945. https://doi.org/10.1038/nmeth.1257.
- (5) Huang, F.; Sirinakis, G.; Allgeyer, E. S.; Schroeder, L. K.; Duim, W. C.; Kromann, E. B.; Phan, T.; Rivera-Molina, F. E.; Myers, J. R.; Irnov, I.; Lessard, M.; Zhang, Y.; Handel, M. A.; Jacobs-Wagner, C.; Lusk, C. P.; Rothman, J. E.; Toomre, D.; Booth, M. J.; Bewersdorf, J. Ultra-High Resolution 3D Imaging of Whole Cells. *Cell* **2016**, *166* (4), 1028–1040. https://doi.org/10.1016/j.cell.2016.06.016.
- (6) Goldwyn, H. J.; Smith, K. C.; Busche, J. A.; Masiello, D. J. Mislocalization in Plasmon-Enhanced Single-Molecule Fluorescence Microscopy as a Dynamical Young's Interferometer. *ACS Photonics* **2018**, *5* (8), 3141–3151. https://doi.org/10.1021/acsphotonics.8b00372.
- (7) Raab, M.; Vietz, C.; Stefani, F. D.; Acuna, G. P.; Tinnefeld, P. Shifting Molecular Localization by Plasmonic Coupling in a Single-Molecule Mirage. *Nat Commun* **2017**, *8* (1), 13966. https://doi.org/10.1038/ncomms13966.
- (8) Fu, B.; Isaacoff, B. P.; Biteen, J. S. Super-Resolving the Actual Position of Single Fluorescent Molecules Coupled to a Plasmonic Nanoantenna. *ACS Nano* **2017**, *11* (9), 8978–8987. https://doi.org/10.1021/acsnano.7b03420.

- (9) Mack, D. L.; Cortés, E.; Giannini, V.; Török, P.; Roschuk, T.; Maier, S. A. Decoupling Absorption and Emission Processes in Super-Resolution Localization of Emitters in a Plasmonic Hotspot. *Nat Commun* **2017**, *8* (1), 14513. https://doi.org/10.1038/ncomms14513.
- (10) Zuo, T.; Goldwyn, H. J.; Isaacoff, B. P.; Masiello, D. J.; Biteen, J. S. Rotation of Single-Molecule Emission Polarization by Plasmonic Nanorods. *J. Phys. Chem. Lett.* **2019**, *10* (17), 5047–5054. https://doi.org/10.1021/acs.jpclett.9b02270.
- (11) Lee, S. A.; Biteen, J. S. Spectral Reshaping of Single Dye Molecules Coupled to Single Plasmonic Nanoparticles. *J. Phys. Chem. Lett.* **2019**, *10* (19), 5764–5769. https://doi.org/10.1021/acs.jpclett.9b02480.
- (12) Xin, L.; Lu, M.; Both, S.; Pfeiffer, M.; Urban, M. J.; Zhou, C.; Yan, H.; Weiss, T.; Liu, N.; Lindfors, K. Watching a Single Fluorophore Molecule Walk into a Plasmonic Hotspot. *ACS Photonics* **2019**, *6* (4), 985–993. https://doi.org/10.1021/acsphotonics.8b01737.
- (13) Zou, N.; Chen, G.; Mao, X.; Shen, H.; Choudhary, E.; Zhou, X.; Chen, P. Imaging Catalytic Hotspots on Single Plasmonic Nanostructures via Correlated Super-Resolution and Electron Microscopy. *ACS Nano* **2018**, *12* (6), 5570–5579. https://doi.org/10.1021/acsnano.8b01338.
- (14) Cheng, X.; Anthony, T. P.; West, C. A.; Hu, Z.; Sundaresan, V.; McLeod, A. J.; Masiello, D. J.; Willets, K. A. Plasmon Heating Promotes Ligand Reorganization on Single Gold Nanorods. *J. Phys. Chem. Lett.* **2019**, *10* (6), 1394–1401. https://doi.org/10.1021/acs.jpclett.9b00079.
- (15) Hamans, R. F.; Parente, M.; Castellanos, G. W.; Ramezani, M.; Gómez Rivas, J.; Baldi, A. Super-Resolution Mapping of Enhanced Emission by Collective Plasmonic Resonances. *ACS Nano* **2019**, *13* (4), 4514–4521. https://doi.org/10.1021/acsnano.9b00132.
- (16) Lee, S. A.; Biteen, J. S. Interplay of Nanoparticle Resonance Frequency and Array Surface Coverage in Live-Cell Plasmon-Enhanced Single-Molecule Imaging. *J. Phys. Chem. C* **2018**, *122* (10), 5705–5709. https://doi.org/10.1021/acs.jpcc.8b01436.
- (17) Jin, D.; Xi, P.; Wang, B.; Zhang, L.; Enderlein, J.; van Oijen, A. M. Nanoparticles for Super-Resolution Microscopy and Single-Molecule Tracking. *Nature Methods* **2018**, *15* (6), 415–423. https://doi.org/10.1038/s41592-018-0012-4.

- (18) Khater, I. M.; Nabi, I. R.; Hamarneh, G. A Review of Super-Resolution Single-Molecule Localization Microscopy Cluster Analysis and Quantification Methods. *Patterns* **2020**, *1* (3), 100038. https://doi.org/10.1016/j.patter.2020.100038.
- (19) Leung, B. O.; Chou, K. C. Review of Super-Resolution Fluorescence Microscopy for Biology. *Appl Spectrosc* **2011**, *65* (9), 967–980. https://doi.org/10.1366/11-06398.
- (20) Whelan, D. R.; Bell, T. D. M. Super-Resolution Single-Molecule Localization Microscopy: Tricks of the Trade. *J. Phys. Chem. Lett.* **2015**, *6* (3), 374–382. https://doi.org/10.1021/jz5019702.
- (21) Thompson, R. E.; Larson, D. R.; Webb, W. W. Precise Nanometer Localization Analysis for Individual Fluorescent Probes. *Biophysical Journal* **2002**, *82* (5), 2775–2783. https://doi.org/10.1016/S0006-3495(02)75618-X.
- (22) Hess, S. T.; Girirajan, T. P. K.; Mason, M. D. Ultra-High Resolution Imaging by Fluorescence Photoactivation Localization Microscopy. *Biophysical Journal* **2006**, *91* (11), 4258–4272. https://doi.org/10.1529/biophysj.106.091116.
- (23) Linde, S. van de; Loschberger, A.; Klein, T.; Heidbreder, M.; Wolter, S.; Heilemann, M.; Sauer, M. Direct Stochastic Optical Reconstruction Microscopy with Standard Fluorescent Probes. *Nature Protocols* **2011**, *6* (7), 991–1010.
- (24) Sharonov, A.; Hochstrasser, R. M. Wide-Field Subdiffraction Imaging by Accumulated Binding of Diffusing Probes. *PNAS* **2006**, *103* (50), 18911–18916. https://doi.org/10.1073/pnas.0609643104.
- (25) Schnitzbauer, J.; Strauss, M. T.; Schlichthaerle, T.; Schueder, F.; Jungmann, R. Super-Resolution Microscopy with DNA-PAINT. *Nat Protoc* **2017**, *12* (6), 1198–1228. https://doi.org/10.1038/nprot.2017.024.
- (26) Glass, A. M.; Liao, P. F.; Bergman, J. G.; Olson, D. H. Interaction of Metal Particles with Adsorbed Dye Molecules: Absorption and Luminescence. *Opt. Lett.*, *OL* **1980**, *5* (9), 368–370. https://doi.org/10.1364/OL.5.000368.
- (27) Weitz, D. A.; Garoff, S.; Hanson, C. D.; Gramila, T. J.; Gersten, J. I. Flourescent Lifetimes and Yields of Molecules Adsorbed on Silver-Island Films. *Journal of Luminescence* **1981**, *24*–*25*, 83–86. https://doi.org/10.1016/0022-2313(81)90226-X.

- (28) Chen, C. Y.; Davoli, I.; Ritchie, G.; Burstein, E. Giant Raman Scattering and Luminescence by Molecules Adsorbed on Ag and Au Metal Island Films. *Surface Science* **1980**, *101* (1), 363–366. https://doi.org/10.1016/0039-6028(80)90631-7.
- (29) Bohren, C. F.; Huffman, D. R. *Absorption and Scattering of Light by Small Particles*; John Wiley & Sons, 2008.
- (30) Rose, A.; Hoang, T. B.; McGuire, F.; Mock, J. J.; Ciracì, C.; Smith, D. R.; Mikkelsen, M. H. Control of Radiative Processes Using Tunable Plasmonic Nanopatch Antennas. *Nano Lett.* **2014**, *14* (8), 4797–4802. https://doi.org/10.1021/nl501976f.
- (31) Li, J.-F.; Li, C.-Y.; F. Aroca, R. Plasmon-Enhanced Fluorescence Spectroscopy. *Chemical Society Reviews* **2017**, *46* (13), 3962–3979. https://doi.org/10.1039/C7CS00169J.
- (32) Akselrod, G. M.; Argyropoulos, C.; Hoang, T. B.; Ciracì, C.; Fang, C.; Huang, J.; Smith, D. R.; Mikkelsen, M. H. Probing the Mechanisms of Large Purcell Enhancement in Plasmonic Nanoantennas. *Nature Photonics* **2014**, *8* (11), 835–840. https://doi.org/10.1038/nphoton.2014.228.
- (33) Lim, K.; Ropp, C.; Barik, S.; Fourkas, J.; Shapiro, B.; Waks, E. Nanostructure-Induced Distortion in Single-Emitter Microscopy. *Nano Lett.* **2016**, *16* (9), 5415–5419. https://doi.org/10.1021/acs.nanolett.6b01708.
- (34) Wertz, E.; Isaacoff, B. P.; Flynn, J. D.; Biteen, J. S. Single-Molecule Super-Resolution Microscopy Reveals How Light Couples to a Plasmonic Nanoantenna on the Nanometer Scale. *Nano Lett.* **2015**, *15* (4), 2662–2670. https://doi.org/10.1021/acs.nanolett.5b00319.
- (35) Blythe, K. L.; Willets, K. A. Super-Resolution Imaging of Fluorophore-Labeled DNA Bound to Gold Nanoparticles: A Single-Molecule, Single-Particle Approach. *J. Phys. Chem. C* **2016**, *120* (2), 803–815. https://doi.org/10.1021/acs.jpcc.5b08534.
- (36) Su, L.; Yuan, H.; Lu, G.; Rocha, S.; Orrit, M.; Hofkens, J.; Uji-i, H. Super-Resolution Localization and Defocused Fluorescence Microscopy on Resonantly Coupled Single-Molecule, Single-Nanorod Hybrids. *ACS Nano* **2016**, *10* (2), 2455–2466. https://doi.org/10.1021/acsnano.5b07294.

- (37) Lin, H.; Centeno, S. P.; Su, L.; Kenens, B.; Rocha, S.; Sliwa, M.; Hofkens, J.; Ujii, H. Mapping of Surface-Enhanced Fluorescence on Metal Nanoparticles Using Super-Resolution Photoactivation Localization Microscopy. *ChemPhysChem* **2012**, *13* (4), 973–981. https://doi.org/10.1002/cphc.201100743.
- (38) Taylor, A. B.; Zijlstra, P. Single-Molecule Plasmon Sensing: Current Status and Future Prospects. *ACS Sens.* **2017**, *2* (8), 1103–1122. https://doi.org/10.1021/acssensors.7b00382.
- (39) Mejía-Salazar, J. R.; Oliveira, O. N. Plasmonic Biosensing. *Chem. Rev.* 2018, 118
 (20), 10617–10625. https://doi.org/10.1021/acs.chemrev.8b00359.
- (40) Wang, Q.; Wang, L. Lab-on-Fiber: Plasmonic Nano-Arrays for Sensing. *Nanoscale* **2020**, *12* (14), 7485–7499. https://doi.org/10.1039/D0NR00040J.
- (41) Wang, D.; Guan, J.; Hu, J.; Bourgeois, M. R.; Odom, T. W. Manipulating Light–Matter Interactions in Plasmonic Nanoparticle Lattices. *Acc. Chem. Res.* **2019**, *52* (11), 2997–3007. https://doi.org/10.1021/acs.accounts.9b00345.
- (42) Taylor, A.; Verhoef, R.; Beuwer, M.; Wang, Y.; Zijlstra, P. All-Optical Imaging of Gold Nanoparticle Geometry Using Super-Resolution Microscopy. *J. Phys. Chem. C* **2018**, *122* (4), 2336–2342. https://doi.org/10.1021/acs.jpcc.7b12473.
- (43) Gómez-Medina, R.; Yamamoto, N.; Nakano, M.; Abajo, F. J. G. de. Mapping Plasmons in Nanoantennas via Cathodoluminescence. *New J. Phys.* **2008**, *10* (10), 105009. https://doi.org/10.1088/1367-2630/10/10/105009.
- (44) Christen, J.; Grundmann, M.; Bimberg, D. Scanning Cathodoluminescence Microscopy: A Unique Approach to Atomic-scale Characterization of Heterointerfaces and Imaging of Semiconductor Inhomogeneities. *Journal of Vacuum Science & Technology B: Microelectronics and Nanometer Structures Processing, Measurement, and Phenomena* **1991**, 9 (4), 2358–2368. https://doi.org/10.1116/1.585704.
- (45) Betzig, E.; Lewis, A.; Harootunian, A.; Isaacson, M.; Kratschmer, E. Near Field Scanning Optical Microscopy (NSOM): Development and Biophysical Applications. *Biophysical Journal* **1986**, *49* (1), 269–279. https://doi.org/10.1016/S0006-3495(86)83640-2.

- (46) Höppener, C.; Siebrasse, J. P.; Peters, R.; Kubitscheck, U.; Naber, A. High-Resolution Near-Field Optical Imaging of Single Nuclear Pore Complexes under Physiological Conditions. *Biophysical Journal* **2005**, *88* (5), 3681–3688. https://doi.org/10.1529/biophysj.104.051458.
- (47) Hakala, T. K.; Rekola, H. T.; Väkeväinen, A. I.; Martikainen, J.-P.; Nečada, M.; Moilanen, A. J.; Törmä, P. Lasing in Dark and Bright Modes of a Finite-Sized Plasmonic Lattice. *Nature Communications* **2017**, *8* (1), 13687. https://doi.org/10.1038/ncomms13687.
- (48) Wang, W.; Ramezani, M.; Väkeväinen, A. I.; Törmä, P.; Rivas, J. G.; Odom, T. W. The Rich Photonic World of Plasmonic Nanoparticle Arrays. *Materials Today* **2018**, *21* (3), 303–314. https://doi.org/10.1016/j.mattod.2017.09.002.
- (49) Willets, K. A.; Wilson, A. J.; Sundaresan, V.; Joshi, P. B. Super-Resolution Imaging and Plasmonics. *Chem. Rev.* **2017**, *117* (11), 7538–7582. https://doi.org/10.1021/acs.chemrev.6b00547.
- (50) Huang, B.; Wang, W.; Bates, M.; Zhuang, X. Three-Dimensional Super-Resolution Imaging by Stochastic Optical Reconstruction Microscopy. *Science* **2008**, *319* (5864), 810–813. https://doi.org/10.1126/science.1153529.
- (51) Biteen, J. S.; Goley, E. D.; Shapiro, L.; Moerner, W. E. Three-Dimensional Super-Resolution Imaging of the Midplane Protein FtsZ in Live Caulobacter Crescentus Cells Using Astigmatism. *ChemPhysChem* **2012**, *13* (4), 1007–1012. https://doi.org/10.1002/cphc.201100686.
- (52) Wriedt, T. Mie Theory: A Review. In *The Mie Theory: Basics and Applications*; Hergert, W., Wriedt, T., Eds.; Springer Series in Optical Sciences; Springer: Berlin, Heidelberg, 2012; pp 53–71. https://doi.org/10.1007/978-3-642-28738-1_2.
- (53) Ropp, C.; Cummins, Z.; Nah, S.; Fourkas, J. T.; Shapiro, B.; Waks, E. Nanoscale Probing of Image-Dipole Interactions in a Metallic Nanostructure. *Nature Communications* **2015**, *6* (1), 6558. https://doi.org/10.1038/ncomms7558.
- (54) Blythe, K. L.; Mayer, K. M.; Weber, M. L.; Willets, K. A. Ground State Depletion Microscopy for Imaging Interactions between Gold Nanowires and Fluorophore-

- Labeled Ligands. *Physical Chemistry Chemical Physics* **2013**, *15* (12), 4136–4145. https://doi.org/10.1039/C2CP43152A.
- (55) Johlin, E.; Solari, J.; Mann, S. A.; Wang, J.; Shimizu, T. S.; Garnett, E. C. Super-Resolution Imaging of Light–Matter Interactions near Single Semiconductor Nanowires. *Nature Communications* **2016**, *7* (1), 13950. https://doi.org/10.1038/ncomms13950.
- (56) Wertz, E. A.; Isaacoff, B. P.; Biteen, J. S. Wavelength-Dependent Super-Resolution Images of Dye Molecules Coupled to Plasmonic Nanotriangles. *ACS Photonics* **2016**, *3* (10), 1733–1740. https://doi.org/10.1021/acsphotonics.6b00344.
- (57) Su, L.; Lu, G.; Kenens, B.; Rocha, S.; Fron, E.; Yuan, H.; Chen, C.; Van Dorpe, P.; Roeffaers, M. B. J.; Mizuno, H.; Hofkens, J.; Hutchison, J. A.; Uji-i, H. Visualization of Molecular Fluorescence Point Spread Functions via Remote Excitation Switching Fluorescence Microscopy. *Nature Communications* **2015**, *6* (1), 6287. https://doi.org/10.1038/ncomms7287.
- (58) Acuna, G. P.; Möller, F. M.; Holzmeister, P.; Beater, S.; Lalkens, B.; Tinnefeld, P. Fluorescence Enhancement at Docking Sites of DNA-Directed Self-Assembled Nanoantennas. *Science* **2012**, *338* (6106), 506–510. https://doi.org/10.1126/science.1228638.
- (59) Takabayashi, S.; P. Klein, W.; Onodera, C.; Rapp, B.; Flores-Estrada, J.; Lindau, E.; Snowball, L.; T. Sam, J.; E. Padilla, J.; Lee, J.; B. Knowlton, W.; Graugnard, E.; Yurke, B.; Kuang, W.; L. Hughes, W. High Precision and High Yield Fabrication of Dense Nanoparticle Arrays onto DNA Origami at Statistically Independent Binding Sites. *Nanoscale* **2014**, *6* (22), 13928–13938. https://doi.org/10.1039/C4NR03069A.
- (60) Thacker, V. V.; Herrmann, L. O.; Sigle, D. O.; Zhang, T.; Liedl, T.; Baumberg, J. J.; Keyser, U. F. DNA Origami Based Assembly of Gold Nanoparticle Dimers for Surface-Enhanced Raman Scattering. *Nature Communications* **2014**, *5* (1), 3448. https://doi.org/10.1038/ncomms4448.
- (61) Su, L.; Lu, G.; Kenens, B.; Rocha, S.; Fron, E.; Yuan, H.; Chen, C.; Van Dorpe, P.; Roeffaers, M. B. J.; Mizuno, H.; Hofkens, J.; Hutchison, J. A.; Uji-i, H. Visualization of Molecular Fluorescence Point Spread Functions via Remote Excitation Switching Fluorescence Microscopy. *Nature Communications* **2015**, *6* (1), 6287. https://doi.org/10.1038/ncomms7287.

- (62) Baiyasi, R.; Jebeli, S. A. H.; Zhang, Q.; Su, L.; Hofkens, J.; Uji-i, H.; Link, S.; Landes, C. F. PSF Distortion in Dye–Plasmonic Nanomaterial Interactions: Friend or Foe? *ACS Photonics* **2019**, *6* (3), 699–708. https://doi.org/10.1021/acsphotonics.8b01576.
- (63) Ringler, M.; Schwemer, A.; Wunderlich, M.; Nichtl, A.; Kürzinger, K.; Klar, T. A.; Feldmann, J. Shaping Emission Spectra of Fluorescent Molecules with Single Plasmonic Nanoresonators. *Phys. Rev. Lett.* **2008**, *100* (20), 203002. https://doi.org/10.1103/PhysRevLett.100.203002.
- (64) Bouillard, J.-S.; Vilain, S.; Dickson, W.; Zayats, A. V. Hyperspectral Imaging with Scanning Near-Field Optical Microscopy: Applications in Plasmonics. *Opt. Express, OE* **2010**, *18* (16), 16513–16519. https://doi.org/10.1364/OE.18.016513.
- (65) Grabinski, C.; Schlager, J.; Hussain, S. Hyperspectral Microscopy for Characterization of Gold Nanoparticles in Biological Media and Cells for Toxicity Assessment. In *Nanomaterial Interfaces in Biology: Methods and Protocols*; Bergese, P., Hamad-Schifferli, K., Eds.; Methods in Molecular Biology; Humana Press: Totowa, NJ, 2013; pp 167–178. https://doi.org/10.1007/978-1-62703-462-3_13.
- (66) Zhang, S.; Reinhard, B. M. Characterizing Large-Scale Receptor Clustering on the Single Cell Level: A Comparative Plasmon Coupling and Fluorescence Superresolution Microscopy Study. *J. Phys. Chem. B* **2019**, *123* (26), 5494–5505. https://doi.org/10.1021/acs.jpcb.9b05176.
- (67) Kaminska, I.; Vietz, C.; Cuartero-González, Á.; Tinnefeld, P.; Fernández-Domínguez, A. I.; Acuna, G. P. Strong Plasmonic Enhancement of Single Molecule Photostability in Silver Dimer Optical Antennas. *Nanophotonics* **2018**, *7* (3), 643–649. https://doi.org/10.1515/nanoph-2017-0081.
- (68) Francisco, A. P.; Botequim, D.; Prazeres, D. M. F.; Serra, V. V.; Costa, S. M. B.; Laia, C. A. T.; Paulo, P. M. R. Extreme Enhancement of Single-Molecule Fluorescence from Porphyrins Induced by Gold Nanodimer Antennas. *J. Phys. Chem. Lett.* **2019**, *10* (7), 1542–1549. https://doi.org/10.1021/acs.jpclett.9b00373.
- (69) Paulo, P. M. R.; Botequim, D.; Jóskowiak, A.; Martins, S.; Prazeres, D. M. F.; Zijlstra, P.; Costa, S. M. B. Enhanced Fluorescence of a Dye on DNA-Assembled Gold

- Nanodimers Discriminated by Lifetime Correlation Spectroscopy. *J. Phys. Chem. C* **2018**, *122* (20), 10971–10980. https://doi.org/10.1021/acs.jpcc.7b12622.
- (70) Barnes, W. L. Fluorescence near Interfaces: The Role of Photonic Mode Density. *Journal of Modern Optics* **1998**, *45* (4), 661–699. https://doi.org/10.1080/09500349808230614.
- (71) Gust, A.; Zander, A.; Gietl, A.; Holzmeister, P.; Schulz, S.; Lalkens, B.; Tinnefeld, P.; Grohmann, D. A Starting Point for Fluorescence-Based Single-Molecule Measurements in Biomolecular Research. *Molecules* **2014**, *19* (10), 15824–15865. https://doi.org/10.3390/molecules191015824.
- (72) Elghanian, R.; Storhoff, J. J.; Mucic, R. C.; Letsinger, R. L.; Mirkin, C. A. Selective Colorimetric Detection of Polynucleotides Based on the Distance-Dependent Optical Properties of Gold Nanoparticles. *Science* **1997**, *277* (5329), 1078–1081. https://doi.org/10.1126/science.277.5329.1078.
- (73) Rosi, N. L.; Mirkin, C. A. Nanostructures in Biodiagnostics. *Chem. Rev.* **2005**, *105* (4), 1547–1562. https://doi.org/10.1021/cr030067f.
- (74) Love, J. C.; Estroff, L. A.; Kriebel, J. K.; Nuzzo, R. G.; Whitesides, G. M. Self-Assembled Monolayers of Thiolates on Metals as a Form of Nanotechnology. *Chem. Rev.* **2005**, *105* (4), 1103–1170. https://doi.org/10.1021/cr0300789.
- (75) Cheng, X.; Lowe, S. B.; Ciampi, S.; Magenau, A.; Gaus, K.; Reece, P. J.; Gooding, J. J. Versatile "Click Chemistry" Approach to Functionalizing Silicon Quantum Dots: Applications toward Fluorescent Cellular Imaging. *Langmuir* **2014**, *30* (18), 5209–5216. https://doi.org/10.1021/la500945f.
- (76) Chen, T.; Dong, B.; Chen, K.; Zhao, F.; Cheng, X.; Ma, C.; Lee, S.; Zhang, P.; Kang, S. H.; Ha, J. W.; Xu, W.; Fang, N. Optical Super-Resolution Imaging of Surface Reactions. *Chem. Rev.* **2017**, *117* (11), 7510–7537. https://doi.org/10.1021/acs.chemrev.6b00673.
- (77) Hauser, M.; Wojcik, M.; Kim, D.; Mahmoudi, M.; Li, W.; Xu, K. Correlative Super-Resolution Microscopy: New Dimensions and New Opportunities. *Chem. Rev.* **2017**, *117* (11), 7428–7456. https://doi.org/10.1021/acs.chemrev.6b00604.

- (78) Blythe, K. L.; Titus, E. J.; Willets, K. A. Triplet-State-Mediated Super-Resolution Imaging of Fluorophore-Labeled Gold Nanorods. *ChemPhysChem* **2014**, *15* (4), 784–793. https://doi.org/10.1002/cphc.201300767.
- (79) Anger, P.; Bharadwaj, P.; Novotny, L. Enhancement and Quenching of Single-Molecule Fluorescence. *Phys. Rev. Lett.* **2006**, *96* (11), 113002. https://doi.org/10.1103/PhysRevLett.96.113002.
- (80) Abadeer, N. S.; Brennan, M. R.; Wilson, W. L.; Murphy, C. J. Distance and Plasmon Wavelength Dependent Fluorescence of Molecules Bound to Silica-Coated Gold Nanorods. *ACS Nano* **2014**, *8* (8), 8392–8406. https://doi.org/10.1021/nn502887j.
- (81) Brongersma, M. L.; Halas, N. J.; Nordlander, P. Plasmon-Induced Hot Carrier Science and Technology. *Nature Nanotechnology* **2015**, *10* (1), 25–34. https://doi.org/10.1038/nnano.2014.311.
- (82) Christopher, P.; Xin, H.; Linic, S. Visible-Light-Enhanced Catalytic Oxidation Reactions on Plasmonic Silver Nanostructures. *Nature Chemistry* **2011**, *3* (6), 467–472. https://doi.org/10.1038/nchem.1032.
- (83) Dhiman, M.; Maity, A.; Das, A.; Belgamwar, R.; Chalke, B.; Lee, Y.; Sim, K.; Nam, J.-M.; Polshettiwar, V. Plasmonic Colloidosomes of Black Gold for Solar Energy Harvesting and Hotspots Directed Catalysis for CO2 to Fuel Conversion. *Chem. Sci.* **2019**, *10* (27), 6594–6603. https://doi.org/10.1039/C9SC02369K.
- (84) Kale, M. J.; Avanesian, T.; Christopher, P. Direct Photocatalysis by Plasmonic Nanostructures. *ACS Catal.* **2014**, *4* (1), 116–128. https://doi.org/10.1021/cs400993w.
- (85) Linic, S.; Aslam, U.; Boerigter, C.; Morabito, M. Photochemical Transformations on Plasmonic Metal Nanoparticles. *Nature Materials* **2015**, *14* (6), 567–576. https://doi.org/10.1038/nmat4281.
- (86) Linic, S.; Christopher, P.; Xin, H.; Marimuthu, A. Catalytic and Photocatalytic Transformations on Metal Nanoparticles with Targeted Geometric and Plasmonic Properties. *Acc. Chem. Res.* **2013**, *46* (8), 1890–1899. https://doi.org/10.1021/ar3002393.
- (87) Sun, M.; Xu, H. A Novel Application of Plasmonics: Plasmon-Driven Surface-Catalyzed Reactions. *Small* **2012**, *8* (18), 2777–2786. https://doi.org/10.1002/smll.201200572.

- (88) Mukherjee, S.; Libisch, F.; Large, N.; Neumann, O.; Brown, L. V.; Cheng, J.; Lassiter, J. B.; Carter, E. A.; Nordlander, P.; Halas, N. J. Hot Electrons Do the Impossible: Plasmon-Induced Dissociation of H2 on Au. *Nano Lett.* **2013**, *13* (1), 240–247. https://doi.org/10.1021/nl303940z.
- (89) Thrall, E. S.; Preska Steinberg, A.; Wu, X.; Brus, L. E. The Role of Photon Energy and Semiconductor Substrate in the Plasmon-Mediated Photooxidation of Citrate by Silver Nanoparticles. *J. Phys. Chem. C* **2013**, *117* (49), 26238–26247. https://doi.org/10.1021/jp409586z.
- (90) Wilson, A. J.; Jain, P. K. Light-Induced Voltages in Catalysis by Plasmonic Nanostructures. *Acc. Chem. Res.* **2020**, *53* (9), 1773–1781. https://doi.org/10.1021/acs.accounts.0c00378.
- (91) Wu, X.; Thrall, E. S.; Liu, H.; Steigerwald, M.; Brus, L. Plasmon Induced Photovoltage and Charge Separation in Citrate-Stabilized Gold Nanoparticles. *J. Phys. Chem. C* **2010**, *114* (30), 12896–12899. https://doi.org/10.1021/jp102720r.
- (92) Andoy, N. M.; Zhou, X.; Choudhary, E.; Shen, H.; Liu, G.; Chen, P. Single-Molecule Catalysis Mapping Quantifies Site-Specific Activity and Uncovers Radial Activity Gradient on Single 2D Nanocrystals. *J. Am. Chem. Soc.* **2013**, *135* (5), 1845–1852. https://doi.org/10.1021/ja309948y.
- (93) Zhou, X.; Choudhary, E.; Andoy, N. M.; Zou, N.; Chen, P. Scalable Parallel Screening of Catalyst Activity at the Single-Particle Level and Subdiffraction Resolution. *ACS Catal.* **2013**, *3* (7), 1448–1453. https://doi.org/10.1021/cs400277a.
- (94) Zou, S.; Schatz, G. C. Narrow Plasmonic/Photonic Extinction and Scattering Line Shapes for One and Two Dimensional Silver Nanoparticle Arrays. *J. Chem. Phys.* **2004**, *121* (24), 12606–12612. https://doi.org/10.1063/1.1826036.
- (95) Zou, S.; Janel, N.; Schatz, G. C. Silver Nanoparticle Array Structures That Produce Remarkably Narrow Plasmon Lineshapes. *J. Chem. Phys.* **2004**, *120* (23), 10871–10875. https://doi.org/10.1063/1.1760740.
- (96) Auguié, B.; Barnes, W. L. Collective Resonances in Gold Nanoparticle Arrays. *Phys. Rev. Lett.* **2008**, *101* (14), 143902. https://doi.org/10.1103/PhysRevLett.101.143902.

- (97) Haynes, C. L.; Van Duyne, R. P. Nanosphere Lithography: A Versatile Nanofabrication Tool for Studies of Size-Dependent Nanoparticle Optics. *J. Phys. Chem. B* **2001**, *105* (24), 5599–5611. https://doi.org/10.1021/jp010657m.
- (98) Flynn, J. D.; Haas, B. L.; Biteen, J. S. Plasmon-Enhanced Fluorescence from Single Proteins in Living Bacteria. *J. Phys. Chem. C* **2016**, *120* (37), 20512–20517. https://doi.org/10.1021/acs.jpcc.5b08049.

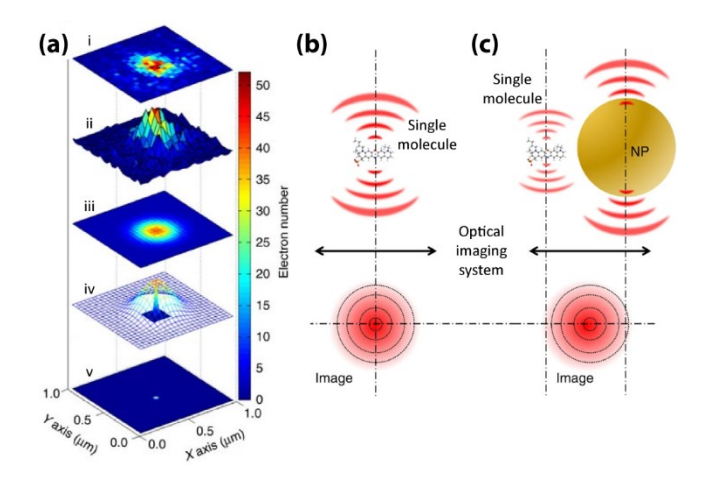


Figure 1. Localization and mislocalization of a fluorophore. (a) Gaussian fit to an experimental single-molecule image. The single molecule is localized to a spot smaller than the diffraction limit. Reproduced from Mack, D. L.; Cortés, E.; Giannini, V.; Török, P.; Roschuk, T.; Maier, S. A. *Nat. Commun.* 2017, 8 (1), 14513 (ref. 9) under a Creative Commons Attribution 4.0 International License (https://creativecommons.org/licenses/by/4.0/). (b) Emission pattern of an isolated molecular emitter. (c) Emission pattern of a coupled molecular emitter-NP system. The dye emission pattern is shifted toward the NP and represents neither the true position of the molecular emitter nor that of the NP. (b, c) Reproduced from Raab, M.; Vietz, C.; Stefani, F. D.; Acuna, G. P.; Tinnefeld, P. *Nat. Commun.* 2017, 8 (1), 13966 (ref. 7) under a Creative Commons Attribution 4.0 International License (https://creativecommons.org/licenses/by/4.0/).

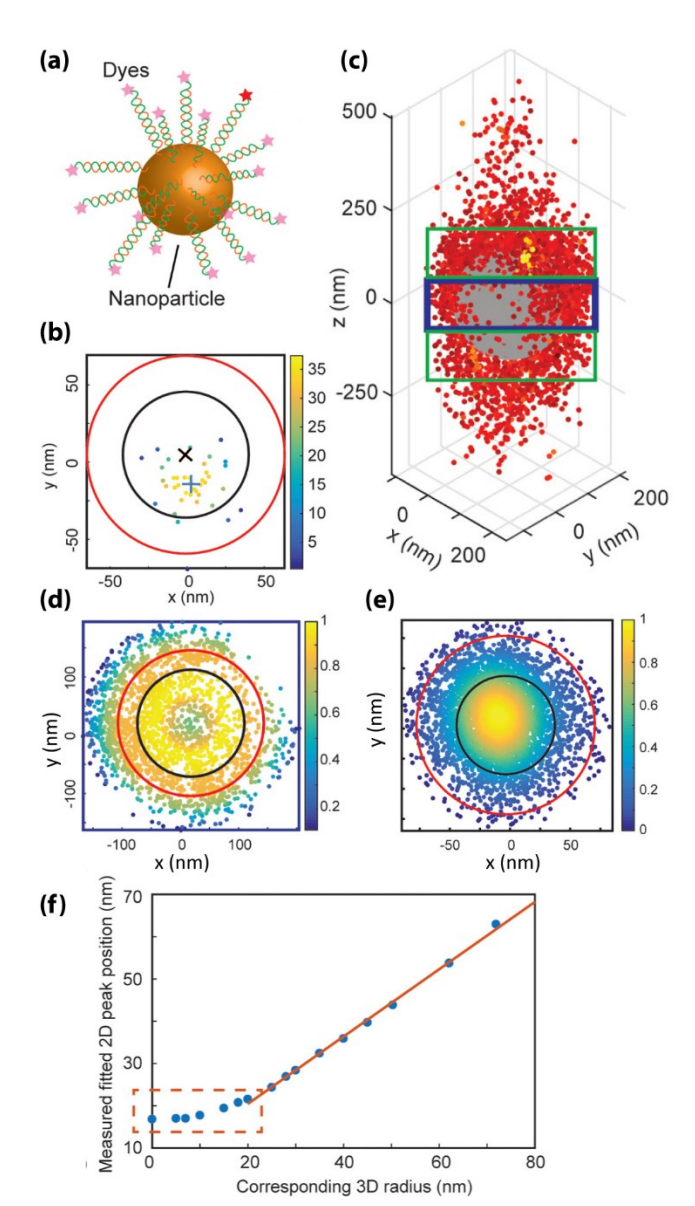


Figure 2. Single-molecule mislocalization around a gold NP. (a) Schematic of the system showing ATTO532 dye molecules attached to a Au NP via rigid dsDNA spacers 11 – 32.6 nm in length. (b) Super-resolved emission from one representative molecule. Each dot is the localization of that same single molecule in one imaging frame. Color bar: density of localizations. The average localization position for that molecule (blue

+) does not match the actual dye molecule positions with 22.8 nm dsDNA spacer (red circle); rather it is mislocalized toward the geometric center of the NP (black ×). The NP has 78.6 nm diameter (black circle). (c) 3D localizations of dye molecules attached to a 179 nm Au NP via 32.6 nm DNA linkers. Each dot represents one localization, color coded by intensity. The blue rectangle indicates the central 150-nm thick slice. (d) *xy* plane projection of localizations in the blue rectangle in 'c' show a ring-shaped localization density. Color bar: normalized density of localizations averaged at each radius according to the circular symmetry of the system. Black circle: Au NP; red circle: actual dye molecule positions. (e) 2D localizations of dye molecules attached to a 78.6 nm Au NP via 32.6 nm DNA linkers. Color bar: normalized density of localizations. Black circle: Au NP; red circle: actual dye molecule positions. (f) Apparent peak positions from fits to the 2D experiments as a function of the actual 3D radius based on simulations. The relationship is linear for radii > 20 nm. (a – f) Reprinted with permission from Fu, B.; Isaacoff, B. P.; Biteen, J. S. *ACS Nano* 2017, *11* (9), 8978–8987 (ref. 8). Copyright 2017 American Chemical Society.

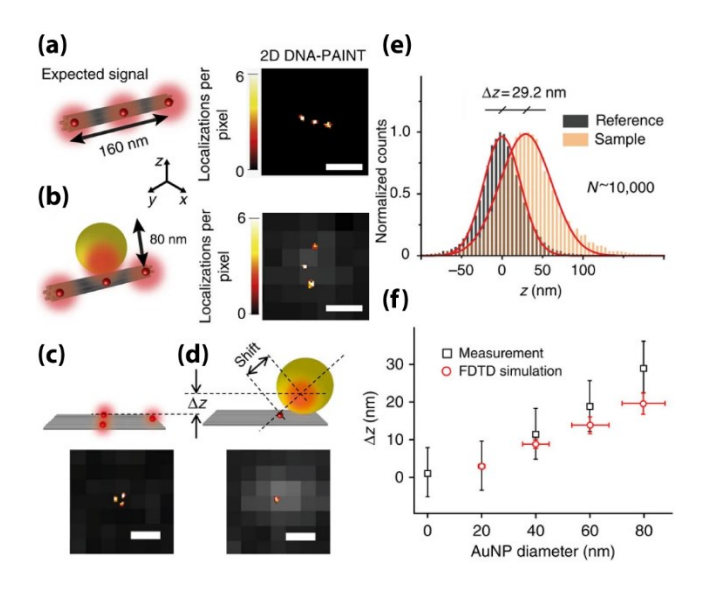


Figure 3. Quantifying mislocalization using DNA origami. (a) Representative DNA-PAINT image of dyes at three docking sites along a 12-helix bundle, as illustrated in the schematic on left. (b) Representative DNA-PAINT image of dyes with a Au NP attached at the center, as illustrated in the schematic on left. (c) Bottom: representative DNA-PAINT image of dyes at three docking sites placed in an equilateral triangle on a DNA origami rectangle, as illustrated in the schematic on top. (d) Bottom: representative DNA-PAINT image of dyes at a docking site 10 nm from a Au NP, as illustrated in the schematic on top. A shift is detected in the emission pattern center and axial position (Δz). (a – d) Scale bars: 200 nm. (e) Experimental axial localization data for fluorophores with (red) and without (black) an 80-nm diameter Au NP. (f) Average experimental (black) and predicted (red) shift (Δz) as a function of Au NP diameter. (a – f) Reproduced from Raab, M.; Vietz, C.; Stefani, F. D.; Acuna, G. P.; Tinnefeld, P. *Nat. Commun.* 2017, 8 (1), 13966 (ref. 7) under a Creative Commons Attribution 4.0 International License (https://creativecommons.org/licenses/by/4.0/).

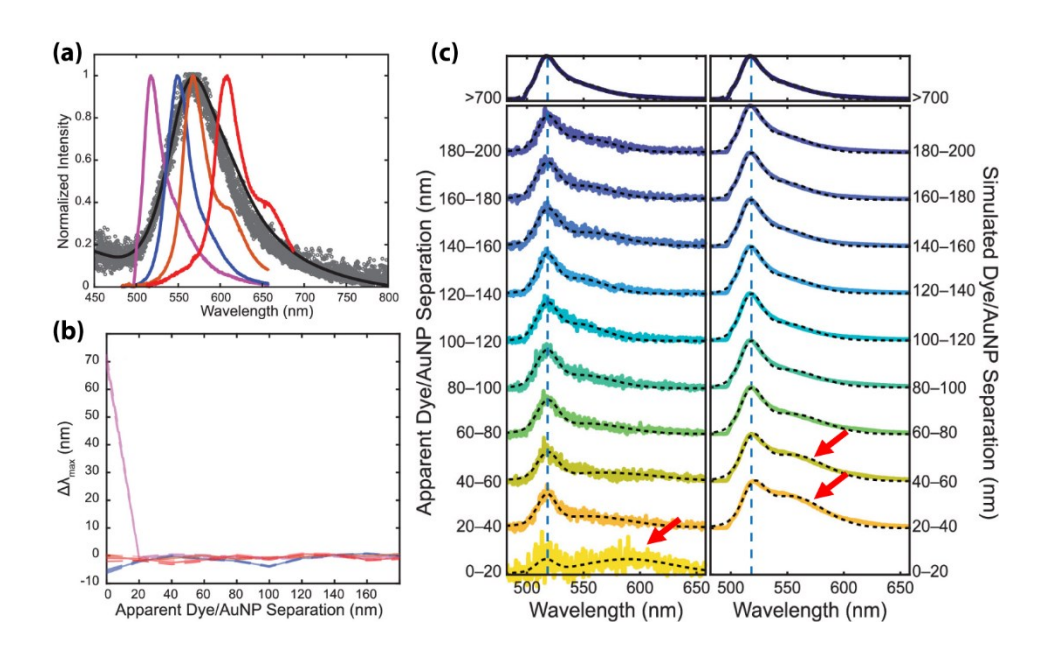


Figure 4. Spectral reshaping of single molecules coupled to plasmonic NPs. (a) Normalized aggregate experimental (gray circles) and simulated (black line) scattering spectra of 95-nm diameter Au NPs. Normalized BDP-FL, BDP-R6G, Cy3, and Cy3.5 emission spectra (magenta, blue, orange, and red, respectively). Excitation wavelength: 488 nm. (b) Shift in maximum emission wavelength as a function of apparent distance between the dye and the NP for BDP-FL, BDP-R6G, Cy3, and Cy3.5 (colors as in 'a'). (c) Average normalized emission spectra for BDP-FL dye molecules at different separation distances from the AuNP. Left: experiments; right: simulations. Top panel: spectrum of uncoupled dyes as in 'a'; this intrinsic emission maximum is indicated by the vertical dashed lines. The red arrows indicate the redder shoulder that is observed on close coupling. (a – c) Reprinted with permission from Lee, S. A.; Biteen, J. S. *J. Phys. Chem. Lett.* **2019**, *10* (19), 5764–5769 (ref. 11). Copyright 2019 American Chemical Society.

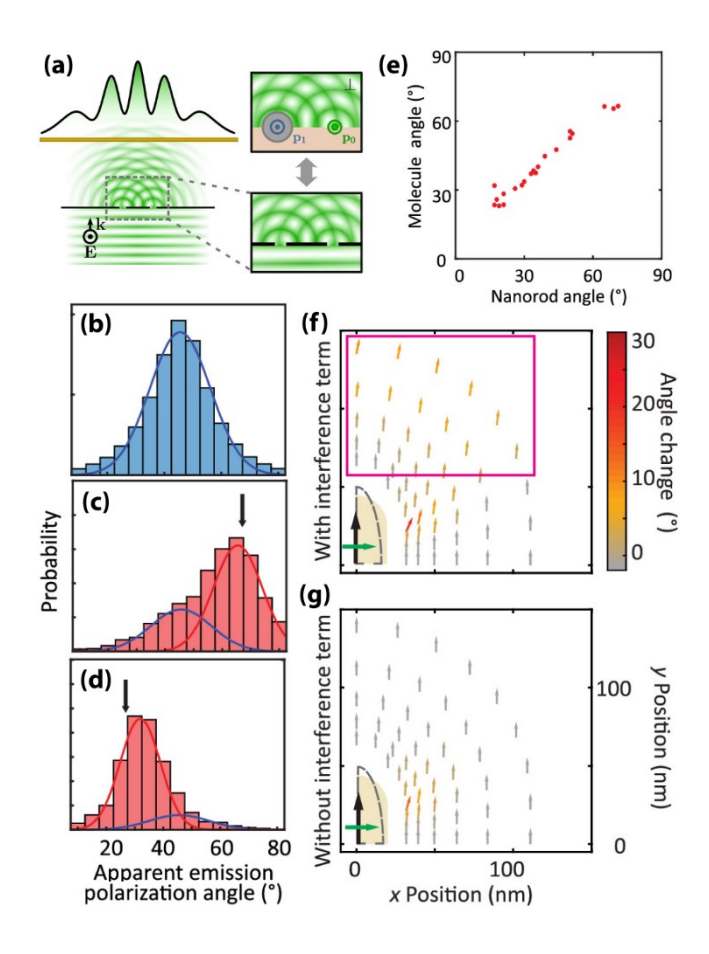


Figure 5. Rotation of single-molecule polarization toward plasmonic dipole. (a) Analogy between (top) the coupling between two dipoles (a grey NP and a green molecular emitter) and (bottom) two slits in Young's double slit experiment. In both cases, spherical waves interfere such that constructive interference appears along rays of equal path length. Reprinted with permission from Goldwyn, H. J.; Smith, K. C.; Busche, J. A.; Masiello, D. J. ACS Photonics **2018**, 5 (8), 3141–3151 (ref. 6). Copyright 2018 American Chemical Society. (b) Emission polarization angle distribution of Cy5.5 dyes measured from single-molecule polarizationresolved microscopy. A random distribution is expected, but experimental bias creates a peak at 45°. (c, d) Emission polarization angle distribution of Cy5.5 dyes near Au nanorods (NRs). The black arrows indicate the measured orientation angle of the NR in each respective experiment. A second peak (red fit) in the distribution is detected near the NR orientation angle. (e) Cy5.5 average polarization angle vs. NR orientation angle. Each point comes from the peak of a red curve as in panels 'c' and 'd'. (f, g) Apparent polarization predictions based on the coupled dipole analytical model for dye molecules near a Au prolate spheroid. The dye molecules are oriented parallel to the longitudinal plasmon mode (black arrow). The interference term is included in (f) and omitted in (g); the pink box indicates positions where interference causes significant polarization rotation. (b - g) Reprinted with permission from Zuo, T.; Goldwyn, H. J.; Isaacoff, B. P.; Masiello, D. J.; Biteen, J. S. J. Phys. Chem. Lett. 2019, 10 (17), 5047–5054 (ref. 10). Copyright 2019 American Chemical Society.

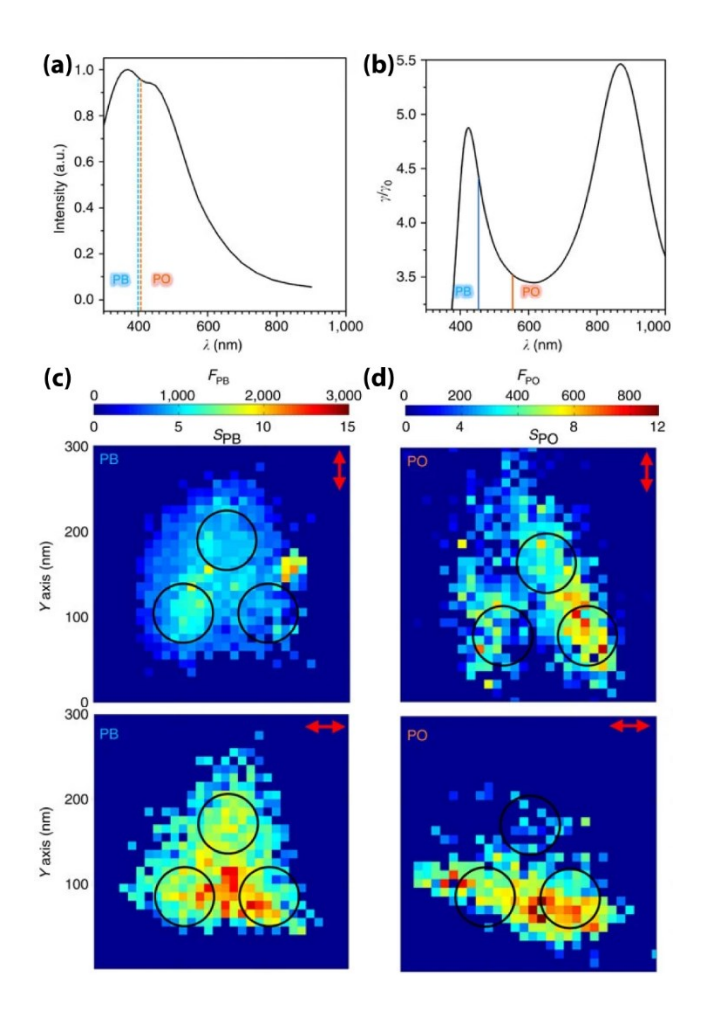


Figure 6. Using single-molecule fluorescence to map electric fields. (a) Simulated scattering spectra of an Al tri-disk system (black) overlaid with the peak absorption wavelengths for Pacific Blue (PB) and Pacific Orange (PO) dyes (blue and orange dashed lines, respectively). (b) Radiative enhancement of the system overlaid with the peak emission wavelengths for PB and PO dyes (blue and orange lines, respectively). PO has a large Stokes shift compared to PB. (c, d) PAINT super-resolution maps of (c) PB and (d) PO adsorbed on the Al tri-disk systems under total internal reflection illumination by a 405-nm laser with polarization orientation indicated by the red arrows. Color bars: fluorescence intensity, *F*, and fluorescent enhancement, *S*. Reproduced from Mack, D. L.; Cortés, E.; Giannini, V.; Török, P.; Roschuk, T.; Maier, S. A. *Nat. Commun.* 2017, 8 (1), 14513 (ref. 9) under a Creative Commons Attribution 4.0 International License (https://creativecommons.org/licenses/by/4.0/).

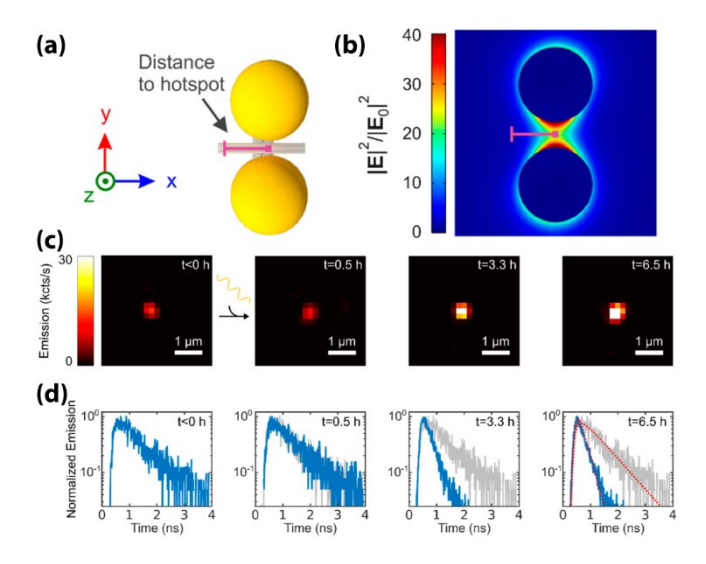


Figure 7. Dynamic fluorescence intensity and lifetime measurements. (a) Schematic of the Au NP dimer and the DNA origami track that runs between. (b) FDTD simulations predict the distribution of the electric field intensity, $|E|^2$, around the dimer. (a, b) Pink line: trajectory of the dye that walks toward the hotspot at the center of the dimer. (c) Fluorescence image of the fluorophore at four time points; the distance from the hotspot decreases with t, the time after beginning walking. The intensity increases as the molecule approaches the hotspot. (d) Fluorescence decay measurements fluorophores in the same device. The lifetime decreases as the molecule approaches the hotspot as evidenced by comparing the measurements (blue) to the decay curve measured at t = 0 (gray). (a – d) Reprinted with permission from Xin, L.; Lu, M.; Both, S.; Pfeiffer, M.; Urban, M. J.; Zhou, C.; Yan, H.; Weiss, T.; Liu, N.; Lindfors, K. ACS Photonics 2019, 6 (4), 985–993. https://pubs.acs.org/doi/10.1021/acsphotonics.8b01737 (ref. 12). Further permissions related to the material excerpted should be directed to the ACS.

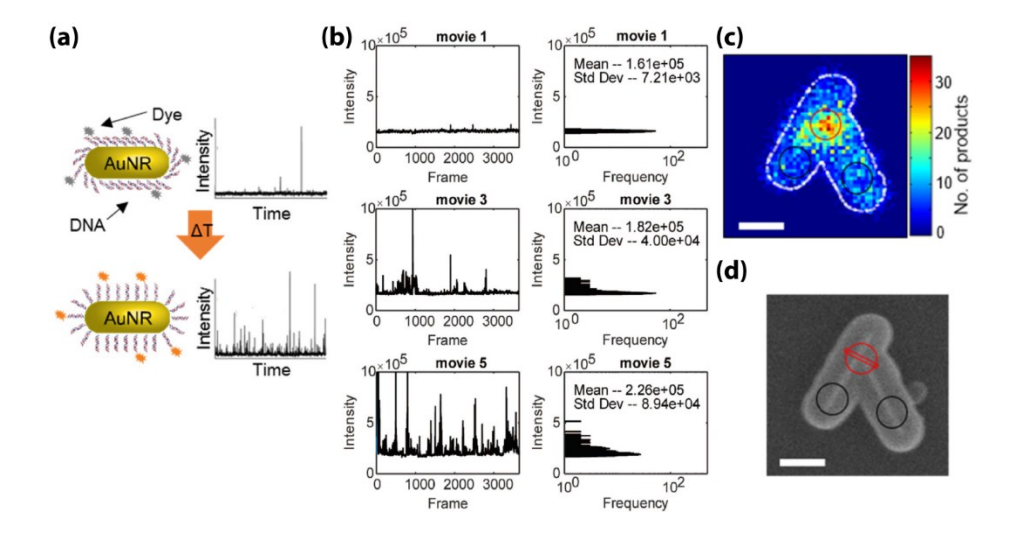


Figure 8. Plasmon-mediated heating and catalysis. (a) Schematic of the system: TAMRA dye molecules are attached to a Au nanorod (NR) via dsDNA spacers. Top: the fluorescence is quenched when the ligands are collapsed; bottom: fluorescence bursts are detected when the ligands are upright. (b) The number of fluorescence bursts (left) and the standard deviation of the intensity (right) for a representative NR increase as a function of elapsed time under laser excitation (from top to bottom). (a – b) Reprinted with permission from Cheng, X.; Anthony, T. P.; West, C. A.; Hu, Z.; Sundaresan, V.; McLeod, A. J.; Masiello, D. J.; Willets, K. A. *J. Phys. Chem. Lett.* 2019, 10 (6), 1394–1401 (ref. 14). Copyright 2019 American Chemical Society. (c) Super-resolution map of catalytic events on a linked Au NR dimer. White line in panel 'c' is the structural contour of the nanostructure from its SEM image in 'd'. (d) SEM image of the same linked Au NR dimer encapsulated in mesoporous silica as in panel 'c'. The red and black circles indicate the gap (hot spot) and non-gap regions. (c – d) Scale bars: 200 nm. Reprinted with permission from Zou, N.; Chen, G.; Mao, X.; Shen, H.; Choudhary, E.; Zhou, X.; Chen, P. *ACS Nano* 2018, 12 (6), 5570–5579 (ref. 13). Copyright 2018 American Chemical Society.

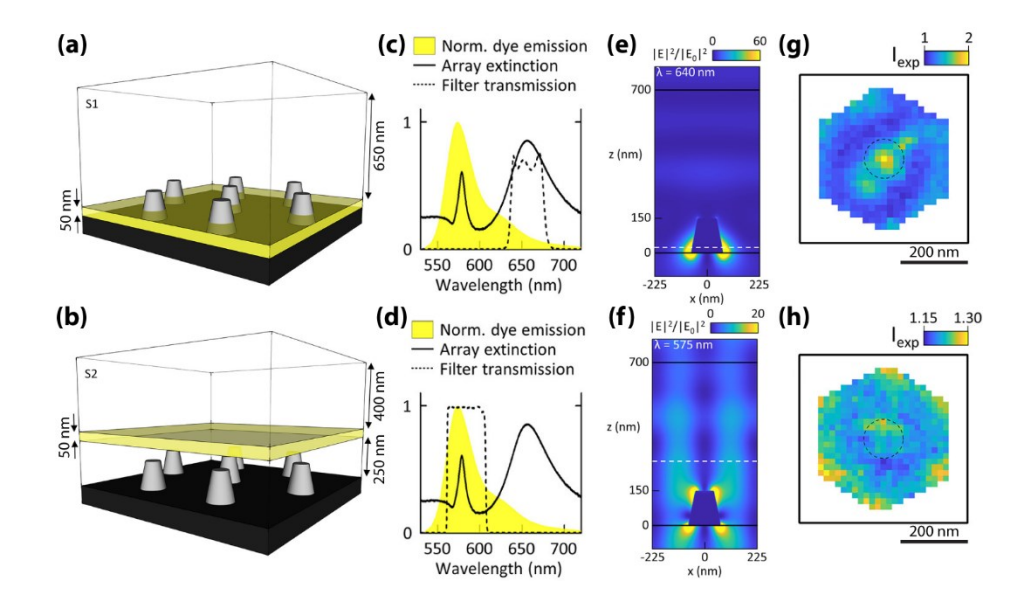


Figure 9. Difference in fluorescence enhancement due to SLR and LSPR. (a, b) Schematic of Al truncated cone array indicting the positioning of the polymer layer doped with a caged dye (yellow) either (a) at the base of the nanocones or, (b) above the plane of the nanocones. (c, d) Normalized dye emission (yellow) and array extinction (solid black line) spectra. Dashed lines indicate the transmission spectra of the emission filters used select for emission at (c) the localized surface plasmon resonance (LSPR) wavelengths and (d) the surface lattice resonance (SLR) wavelengths. (e, f) Cross-section view of the calculated electric field intensity, $|E|^2$, around the nanocone at the peak wavelength of (e) the LSPR and (f) the SLR (640 and 575 nm, respectively, based on the extinction spectrum in panels 'c' and 'd'). (g, h) 2D histogram of the average experimentally observed emission enhancement, I_{exp} , in each 22 nm × 22 nm pixel at (g) the LSPR wavelengths and (h) the SLR wavelengths. The dashed line denotes the base of the nanostructure. (a – h) Reprinted with permission from Hamans, R. F.; Parente, M.; Castellanos, G. W.; Ramezani, M.; Gómez Rivas, J.; Baldi, A. *ACS Nano* 2019, 13 (4), 4514–4521 (ref. 15). Copyright 2019 American Chemical Society.

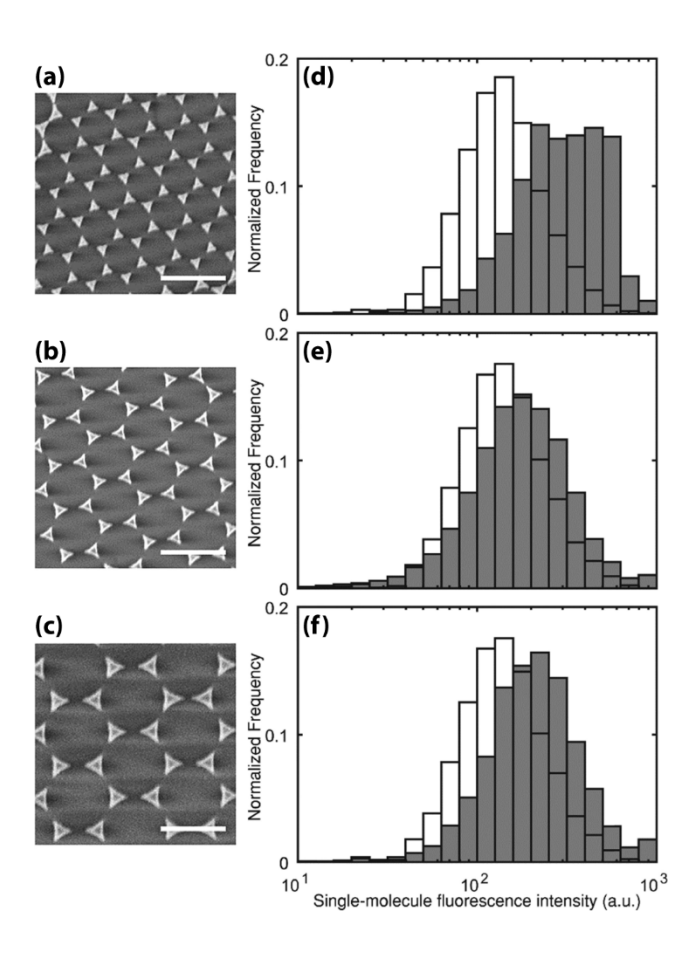


Figure 10. Fluorescence enhancement in live-cell imaging. (a – c) Electron micrographs of nanotriangle arrays made by nanosphere lithography using spheres of diameters (a) 500 nm, (b) 750 nm, and (c) 1000 nm. (a – e) Scale bars: 1 μm. (d – f) Fluorescence intensity distributions of membrane-bound TcpP-PAmCherry molecules in *V. cholerae* cells imaged on glass coverslips (white) and on nanotriangle-coated coverslips (gray) with sizes corresponding to panels 'a', 'b', and 'c', respectively. (a – f) Reprinted with permission from Lee, S. A.; Biteen, J. S. *J. Phys. Chem. C* 2018, *122* (10), 5705–5709 (ref. 16). Copyright 2018 American Chemical Society.